Dalton Transactions

ROYAL SOCIETY OF CHEMISTRY

PAPER

View Article Online
View Journal | View Issue

Cite this: *Dalton Trans.*, 2026, **55**, 5571

Enhanced MMLCT character in thiol-bridged Pt(II) dimers featuring tridentate cyclometalating ligands

Sarah Kromer, Liam J. Dress, Evgeny O. Danilov, Livia I. Cohen, Adrienne P. Faulkner and Felix N. Castellano *

Thiol–pyridine and thiol–quinoline bridging ligands have previously been shown to reduce the metal–metal separation in Pt(II) dimers. Additionally, coordination complexes of the tridentate cyclometalating ligand 4-tolyl-6-phenyl-2,2′-bipyridine (4tpbpy) exhibit enhanced Pt d_{z^2} orbital overlap through improved π-stacking of the cyclometalating ligands (CMLs), lengthening the Pt–Pt distance at which metal–metal-to-ligand charge transfer (MMLCT) transitions can be observed. To collectively study these phenomena, a series of molecules using the 4tpbpy CML with thiol-containing bridges: 2-benzothiazolethiol (**2**), 2-quinolinethiol (**3**), 2-pyridinethiol (**4**), and 6-methyl-2-pyridinethiol (**5**), was synthesized. Their photophysical properties were compared with a model complex known to exhibit MMLCT photophysics within the same tridentate motif, $[Pt_2(4tbpy)_2(\mu\text{-dppm})][PF_6]_2$ (**1**) (dppm = bis(diphenylphosphino)methane). The MMLCT energies in **2–5** were significantly lower than in **1** and in similar bidentate systems, as evidenced by red-shifted absorption bands extending past 650 nm and photoluminescence (PL) maxima between 750–790 nm. Femtosecond transient absorption spectroscopy showed that the population and subsequent relaxation of the ^{3}MMLCT excited state in **2–5** are similar to those in **1**, with noticeably reduced time constants. The growth of the ^{3}MMLCT excited state in **2–5** was observed with a shortened time constant of ~55 ps, which subsequently relaxes on the timescale of 2–7 ns, atypical for these triplet charge transfer excited states.

Received 15th February 2026,
Accepted 17th March 2026

DOI: 10.1039/d6dt00411c

rsc.li/dalton

Introduction

Vibronic coherence was first observed in Pt(II) dimers in tetrakis(μ-pyrophosphito)diplatinate(II), or Pt(POP), and has since been extensively studied to glean insight into the phenomenon.[1–8] Vibronic coherence in cyclometalated Pt–Pt dimers featuring various ligand structures has also been investigated to determine how the ligand manifold affects the propagation of the coherent vibrational wavepacket (CVWP).[9–24] Understanding the role of the Pt(II) dimer structure in the CVWP progression is proposed to guide the design of molecules poised for solar energy harvesting and to enable structural tuning of photochemical and photophysical reaction pathways.[25]

A general requirement of Pt(II) dimers intended to probe vibronic coherence phenomena is a sufficiently short Pt–Pt distance, such that orbital splitting causes the lowest-energy transition to be termed metal–metal-to-ligand charge transfer (MMLCT). A consequence of this splitting is the presence of two nearly isoenergetic transitions of [dσ* → in-phase π*] and [dσ* → out-of-phase π*] character (Fig. 1). Colloquially,

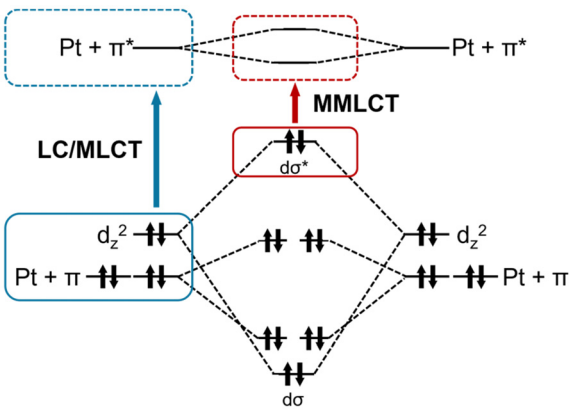

Fig. 1 Molecular orbital diagram highlighting orbital contributions to ligand-centred/metal-to-ligand charge transfer (LC/MLCT) *versus* MMLCT transitions.

Department of Chemistry, North Carolina State University, Raleigh, NC 27695-8204, USA. E-mail: fncastel@ncsu.edu

MMLCT usually refers to the [dσ* → in-phase π*] transition only and will be referred to as such here. MMLCT transitions appear at lower energies than the mixed ligand-centered/metal-to-ligand charge transfer (LC/MLCT) [$\pi/d_{z^2} \rightarrow \pi^*$] transition in complexes with negligible metal–metal interactions. As a result, the energy of the MMLCT features serves as a benchmark for a dimer's orbital overlap and, consequently, a rough estimate of the Pt–Pt distance, with lower-energy transitions considered more favorable for the study of vibronic coherence.

Numerous studies have examined Pt(II) dimers to alter orbital overlap by modifying ligand structure, from which it was determined that both bridging and cyclometalating ligands (CMLs) affect the Pt–Pt distance.[26–47] Overall, the shortest reported Pt–Pt distances were observed in molecules cyclometalated by benzoquinoline (bzq) and bridged by substituted 2-hydroxypyridines (2.82–2.86 Å).[28] By comparison, bridging with analogous 2-thiolpyridine and 2-thiolquinoline motifs is more synthetically facile, and Pt–Pt distances can approach the metal–metal distances achieved with hydroxypyridine with sufficient ligand modification. Specifically, utilizing 2-phenylpyridine (ppy), a Pt–Pt distance of 2.97 Å was achieved with the 2-benzothiazolethiol bridge.[48,49] This distance was reduced to 2.85 Å using 2-pyridinethiol, consistent with complexes bridged by hydroxypyridines.[50] Increasing the steric bulk of the bridge by instead using 6-methyl-2-pyridinethiol red-shifts spectral features, suggesting enhanced metal–metal interaction, though X-ray crystal structures are not reported for direct quantitative comparisons of Pt–Pt distances.[30] While further red-shifted PL features are observed in complexes cyclometalated by 1-phenylisoquinoline (piq), the comparable Pt–Pt distances to those reported in complexes of ppy and bzq suggest this results from the extension of the CML π-system rather than a change in the Pt orbital overlap.[46]

Another method of reducing the Pt–Pt distance is to extend the CML π-system. Previous literature demonstrates that the tridentate CML, 4-tolyl-6-phenyl-2,2′-bipyridine (4tpbpy), in Pt(II) dimers allows more direct head-on overlap between metal d_{z^2} orbitals through enhanced π-stacking, thereby lengthening the distance required for MMLCT photophysics.[33,39,40] A recent publication from our research group used 4tpbpy and diphosphine bridging ligands with various carbon chain lengths, demonstrating that the onset of MMLCT features occurred at longer Pt–Pt distances than in the corresponding bidentate systems.[33] Despite a recent increase in investigations into the photophysics of Pt(II) dimers with tridentate cyclometalating ligands,[33,41–43,45] comparatively little is known about the effects of bridging ligand modification compared to commensurate bidentate motifs.

To probe these phenomena concurrently, this investigation reports four novel Pt(II) dimer complexes utilizing the 4tpbpy CML and bridged by varying thiol-containing motifs: $[Pt_2(4tbpy)_2(\mu\text{-R})][PF_6]$, where R = 2-benzothiazolethiol (**2**), 2-quinolinethiol (**3**), 2-pyridinethiol (**4**), and 6-methyl-2-pyridinethiol (**5**), (Fig. 2). The impact of these structural modifications was analysed by static and time-resolved spectroscopic methods, and the resulting spectra were compared with a model complex, $[Pt_2(4tbpy)_2(\mu\text{-bis(diphenylphosphino)methane})][PF_6]_2$ (**1**), previously established to exhibit MMLCT photophysics.[33,39,40] In prior reports, DFT and TD-DFT calculations, combined with spectroscopic data, revealed that **1** exhibits sufficient orbital overlap to feature MMLCT absorption and PL maxima at 475 nm and 677 nm, respectively, in THF. Here, those features were recorded in MeCN, where the PL maximum red-shifted slightly to 680 nm. Molecules **2–5** show further bathochromic shifts; the MMLCT absorption is centred at ~550 nm with a tail extending past 650 nm, and PL maxima between 775 and 795 nm. In the MMLCT excited-state manifold, a process mirroring the ^{1}MMLCT → ^{3}MMLCT intersystem crossing (ISC) in **1** was observed from **2–5** with time constants ranging from 52 to 59 ps. Finally, the ^{3}MMLCT excited-state lifetimes of **2–5** were measured to be 2–7 ns, compared to 216 ns in **1**. Overall, the spectral progression of the novel thiol-bridged dimers is comparable to that of **1**, with substantially red-shifted spectral features and rapid excited-state deactivation. While reduced spectral feature energies are a contributing factor in the increased rates of excited-state processes, in agreement with the energy gap law, additional mechanisms must be considered – such as reduced symmetry – through further spectroscopic and theoretical examination.

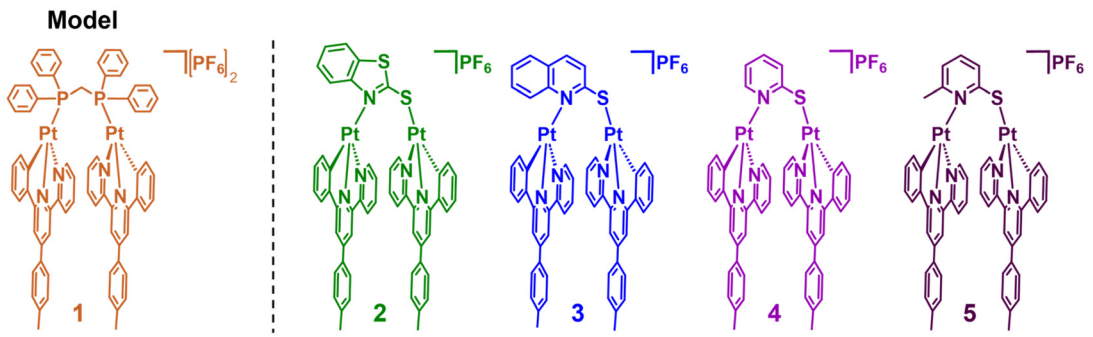

Fig. 2 Chemical structures of model complex **1** with the thiol-bridged complexes **2–5**.

Experimental

General procedures

All solvents and starting reagents were acquired and used as received from VWR, Fisher Scientific, Ambeed, and Sigma-Aldrich. NMR spectroscopy was completed utilizing deuterated solvents purchased from VWR; ^{1}H NMR experiments were conducted on a Bruker Avance 400 MHz spectrometer. The MNova 10.0 software package was used to process NMR data by referencing peaks to residual solvent signals and determining peak integrations. Characterization by mass spectrometry was performed at the Michigan State University Mass Spectrometry Core (East Lansing, MI) (TOF-MS-ES+), and elemental analyses were conducted by Atlantic Microlab, Inc. in Norcross, GA. All spectra of previously prepared molecules matched prior reports.[33,39,40] NMR and mass spectra of novel complexes are presented in Fig. S1–S8.

Synthesis

All reactions reported here were performed under N_2 atmosphere; however, none of the reported intermediates or final dimer complexes are sensitive to oxygen. The cyclometalating ligand, 4-tolyl-6-phenyl-2,2′-bipyridine (**4tpbpy**), the associated Pt(II) monomer starting material, **[Pt(4tpbpy)Cl]**, and model complex **1** were prepared according to literature methods.[33,39,40,51,52] The synthesis of **2–5** utilized the same general procedure.[39] **[Pt(4tpbpy)Cl]** (2 equiv.) and the requisite bridging ligand (1 equiv.) were dissolved in a 2 : 1 mixture of MeCN : MeOH. To this mixture, potassium *tert*-butoxide (1.2 equiv.) was added, and stirred overnight under N_2 at 50 °C (**2**) or room temperature (**3–5**). If necessary, the reaction was cooled to room temperature, and the mixture was vacuum filtered to remove unreacted starting materials. The filtrate was then collected, and metathesis was performed by adding excess NH_4PF_6 dissolved in methanol (10–25 equiv.). After stirring for 10 min, the mixture was dried by rotary evaporation. The solid residue was dissolved in a minimal amount of DCM and then added to a stirred solution of diethyl ether, resulting in the precipitation of a dark-coloured solid. The product was collected by vacuum filtration, then washed with diethyl ether and H_2O. If necessary, further purification can be achieved by vapor diffusion of diethyl ether into a concentrated solution of the product in MeCN, or by neutral alumina column chromatography using a 5% MeCN/95% DCM liquid phase, in which the dark band is collected.

[Pt$_2$(4-tolyl-6-phenyl-2,2′-bipyridine)(μ-2-benzothiazolethiol)][PF$_6$] (2). 103 mg of **[Pt(4tpbpy)Cl]** (0.186 mmol, 1.7 equiv.), 18.5 mg 2-benzothiazolethiol (0.11 mmol, 1 equiv.), and 15 mg of potassium *tert*-butoxide (0.13 mmol, 1.2 equiv.) were dissolved in 15 mL of a 2 : 1 mixture of MeCN/MeOH and heated to 50 °C under N_2 overnight. Ion exchange was performed with 5 mL of saturated NH_4PF_6/MeOH solution (9 equiv.). A purple solid was collected by recrystallization from dichloromethane and diethyl ether (112 mg, 0.08 mmol, 90% yield). ^{1}H NMR (400 MHz, CD_3CN) (Fig. S1): 8.36 (d, J = 5.3 Hz, 1H), 8.05 (d, J = 8.1 Hz, 1H), 7.88 (m, 3H), 7.80 (d, J = 7.7 Hz, 1H), 7.71 (d, J = 7.9 Hz, 2H), 7.52 (s, 1H), 7.48–7.44 (m, 3H), 7.42–7.37 (m, 4H), 7.33–7.21 (m, 7H), 7.16 (t, J = 6.2 Hz, 1H), 7.12 (d, J = 7.6 Hz, 1H), 7.05 (d, J = 7.4 Hz, 1H), 6.99 (d, J = 7.6 Hz, 1H), 6.85 (t, J = 7.4 Hz, 1H), 6.79 (t, J = 7.4 Hz, 1H), 6.62 (t, J = 7.4 Hz, 2H), 6.15 (d, J = 7.1 Hz, 1H), 2.47 (s, 3H), 2.46 (s, 3H). TOF-MS-ES+ (CH_2Cl_2) m/z: 1 198.1882 $[M\text{-}PF_6]^+$, calcd ($C_{53}H_{38}N_5Pt_2S_2$) 1198.1860 (Fig. S2). Elemental analysis (%) calcd for $C_{53}H_{38}F_6N_5PPt_2S_2{\cdot}1H_20$: C, 46.73; H, 2.96; N, 5.14. Found: C, 46.69; H, 2.70; N, 5.09.

[Pt$_2$(4-tolyl-6-phenyl-2,2′-bipyridine)(μ-2-quinolinethiol)][PF$_6$] (3). 54 mg of **[Pt(4tpbpy)Cl]** (0.098 mmol, 2.0 equiv.), 8.08 mg of 2-quinolinethiol (0.050 mmol, 1.0 equiv.), and 6.1 mg of potassium *tert*-butoxide (0.054 mmol, 1.1 equiv.). Ion exchange was performed with 5 mL of a saturated solution of NH_4PF_6 in methanol (17 equiv.). A blue/green solid was collected by vacuum filtration (45 mg, 0.034 mmol, 69% yield). ^{1}H NMR (400 MHz, CD_3CN) (Fig. S3): δ 9.08 (t, J = 5.3 Hz, 1H), 8.33 (d, J = 5.1 Hz, 1H), 8.11 (d, J = 8.8 Hz, 1H), 8.00 (d, J = 8.7 Hz, 1H), 7.93–7.85 (m, 3H), 7.82 (d, J = 7.7 Hz, 1H), 7.76 (d, J = 7.9 Hz, 1H), 7.68 (d, J = 5.1 Hz, 1H), 7.56–7.50 (m, 4H), 7.45–7.40 (m, 4H), 7.39 (s, 2H), 7.30 (d, J = 8.0 Hz, 2H), 7.27 (d, J = 8.1 Hz, 2H), 7.17 (t, J = 6.5 Hz, 1H), 7.12–7.03 (m, 4H), 6.82 (t, J = 7.4 Hz, 2H), 6.59 (q, J = 6.3 Hz, 2H), 6.08 (d, J = 7.5 Hz, 1H), 2.49 (s, 3H), 2.47 (s, 3H). TOF-MS-ES+ (CH_2Cl_2) m/z: 1192.2294 $[M\text{-}PF_6]^+$, calcd ($C_{55}H_{40}N_5Pt_2S$) 1192.2297 (Fig. S4). Elemental analysis (%) calcd for $C_{55}H_{40}F_6N_5PPt_2S{\cdot}1CH_2Cl_2$: C, 47.26; H, 2.97; N, 4.92. Found: C, 47.59; H, 2.80; N, 4.94.

[Pt$_2$(4-tolyl-6-phenyl-2,2′-bipyridine)(μ-2-pyridinethiol)][PF$_6$] (4). 52 mg **[Pt(4tpbpy)Cl]** (0.094 mmol, 2.1 equiv.), 5.03 mg of 2-pyridinethiol (0.045 mmol, 1.0 equiv.), and 5.3 mg of potassium *tert*-butoxide (0.047 mmol, 1.0 equiv.) dissolved in MeCN/MeOH. Ion exchange was performed with 5 mL of saturated NH_4PF_6 in methanol (18 equiv.). A blue/green solid was collected by vacuum filtration (57 mg, 0.044 mmol, 94% yield). ^{1}H NMR (400 MHz, CD_3CN) (Fig. S5): δ 8.51 (d, J = 5.6 Hz, 1H), 8.30 (d, J = 5.4 Hz, 1H), 8.03–7.96 (m, 2H), 7.90 (t, J = 7.5 Hz, 1H), 7.86 (t, J = 7.8 Hz, 1H), 7.72 (t, J = 8.6 Hz, 2H), 7.66 (t, J = 7.6 Hz, 1H), 7.50–7.43 (m, 4H), 7.42–7.35 (m, 3H), 7.30–7.22 (m, 7H), 7.08 (m, 3H), 6.94 (d, J = 7.5 Hz, 1H), 6.86 (t, J = 7.5 Hz, 2H), 6.58 (t, J = 7.3 Hz, 2H), 6.12 (d, J = 7.5 Hz, 1H), 2.48 (s, 3H), 2.46 (s, 3H). TOF-MS-ES+ (CH_2Cl_2) m/z: 1142.2141 $[M\text{-}PF_6]^+$, calcd ($C_{51}H_{38}N_5Pt_2S$) 1142.2140 (Fig. S6). Elemental analysis (%) calcd for $C_{51}H_{38}F_6N_5PPt_2S{\cdot}0.5CH_2Cl_2$: C, 46.49; H, 2.95; N, 5.26. Found: C, 46.48; H, 2.81; N, 5.31.

[Pt$_2$(4-tolyl-6-phenyl-2,2′-bipyridine)(μ-6-methyl-2-pyridinethiol)][PF$_6$] (5). 47 mg of **[Pt(4tpbpy)Cl]** (0.0852 mmol, 1.9 equiv.), 5.67 mg of 6-methyl-2-pyridinethiol (0.045 mmol, 1.0 equiv.), and potassium *tert*-butoxide (5.22 mg, 0.047 mmol, 1.0 equiv.). Ion exchange was performed with 191 mg of NH_4PF_6 in 10 mL of MeCN (1.17 mmol, 25 equiv.). After precipitation in diethyl ether, 0.046 g of purple/black solid was collected (0.035 mmol, 84% yield). ^{1}H NMR (400 MHz, CD_3CN) (Fig. S7): δ 8.39 (d, J = 5.4 Hz, 1H), 7.99–7.90 (m, 4H), 7.82 (t, J = 8.6 Hz, 2H), 7.65 (t, J = 7.8 Hz, 1H), 7.60–7.52 (m, 4H), 7.46–7.42 (m, 3H), 7.39 (d, J = 2.0 Hz, 1H), 7.35–7.30 (m, 3H), 7.30–7.23 (m, 4H), 7.12 (d, J = 7.9 Hz, 2H), 7.08 (d, J = 7.7 Hz, 1H), 6.89 (t, J = 7.3 Hz, 1H),

6.87 (t, J = 7.4 Hz, 1H), 6.67 (t, J = 7.5 Hz, 1H), 6.64 (t, J = 7.5 Hz, 1H), 6.11 (d, J = 7.5 Hz, 1H), 2.67 (s, 3H), 2.50 (s, 3H), 2.46 (s, 3H). TOF-MS-ES+ (CH_2Cl_2) m/z: 1156.2267 $[M\text{-}PF_6]^+$, calcd ($C_{52}H_{40}N_5Pt_2S$) 1156.2295 (Fig. S8). Elemental analysis (%) calcd for $C_{52}H_{40}F_6N_5PPt_2S$: C, 47.97; H, 3.10; N, 5.38. Found: C, 48.09; H, 3.18; N, 5.27.

Steady state spectroscopy

UV-vis spectra were collected on a Cary 60 spectrophotometer. An Edinburgh FS920 fluorometer was utilized to measure static photoluminescence (PL) spectra following excitation into the lowest energy MMLCT absorption band. Samples for steady-state PL were prepared in a 1 cm quartz cuvette with the optical density at excitation maintained at 0.2.

Time-resolved photoluminescence

Time-resolved PL decays of **1** were collected with the nanosecond transient absorption setup, described below. PL decays of **2–5** were collected using a LifeSpec II TCSPC, and excitation was provided by the 80 MHz output of a Chameleon Ti:sapphire Oscillator. The Chameleon OPO was tuned to 570 nm with a pulse power of 0.2 nJ per pulse. Samples were prepared in a 1 cm quartz cuvette with optical density maintained between 0.3 and 0.4, and integrity was monitored by UV-vis collected before and after laser exposure.

Nanosecond transient absorption spectroscopy (nsTAa)

The nsTA difference spectra, as well as single-wavelength kinetic photoluminescence and absorption decays of **1** were collected with an Edinburgh LP920 flash photolysis system coupled with a Vibrant 355 LD-UVM Nd:YAG/OPO from OPOTEK. The OPO was electronically controlled by the Edinburgh L900 software. Difference spectra were collected by an Andor Technology iStar ICCD camera, and single-wavelength kinetic decays were measured utilizing a Hamamatsu R2658P PMT detector. The sample was measured in a 1 cm cuvette with an optical density of 0.2 at excitation. The solution was prepared in a glovebox with an inert N_2 environment and was monitored by UV-vis before and after experiment.

Femtosecond transient absorption spectroscopy (fsTA)

fsTA was measured at the IMAKS facility at NC State University. The pump and probe pulses were generated by splitting the 1 kHz output from a Coherent Astrella Ti:sapphire regenerative amplifier into separate beams. The pump pulse was directed into a Coherent OperA Solo and tuned to the desired excitation wavelength. An optical chopper operating at 500 Hz was utilized to block every other pulse. The probe beam was first directed into a 6 ns Newport optical delay stage, then the white light continuum was generated by striking a CaF_2 crystal. The pump and probe beams were overlapped inside a Helios Spectrometer from Ultrafast Systems, and data collection utilized a fiber optic connected to a linear array detector. Samples were measured with optical densities at excitation between 0.2 and 0.3 in a 2 mm cuvette. All samples were stirred during laser exposure, and UV-vis spectra were collected before and after experimentation to ensure sample integrity was maintained.

Results and discussion

Synthesis

Novel complexes **2–5** were successfully prepared using modified published procedures.[39] The target complex was collected with 70–94% yields, and characterized by ^{1}H NMR, mass spectrometry, and elemental analysis, whose spectra are presented in Fig. S1–S8.

Absorption spectroscopy

In the absence of single crystal X-ray structures, a facile means of estimating metal separations in Pt(II) dimers is from the energy of the most bathochromic absorption band, where lower energy features suggest shorter metal–metal distances. The lowest energy band of **1** is centered near 475 nm (Fig. 3) in MeCN and was confirmed to be the [dσ* → in-phase π*] MMLCT transition by TD-DFT in a previous report.[33] In comparison, the lowest energy absorbance in **2–5** in MeCN is centered at 550 nm, with a tail extending to 650 nm in **2–4** and 700 nm in **5** (Fig. 3), and is also assumed to be the [dσ* → in-phase π*] transition. While the absorption energies of **2–5** are similar, **5** shows the most red-shifted feature, potentially exhibiting the shortest Pt–Pt distance in the series. Overall, the substantial bathochromic shift in **2–5** compared to **1** suggests a significant reduction in Pt–Pt distance in the newly prepared complexes. Notably, there is an additional band in the spectrum of **2** at 400 nm and an increase in intensity of **3** at 340 nm compared to the other complexes. This could result from additional transitions involving the extended π-systems of their respective bridging ligands, but must be confirmed by TD-DFT electronic-structure calculations.

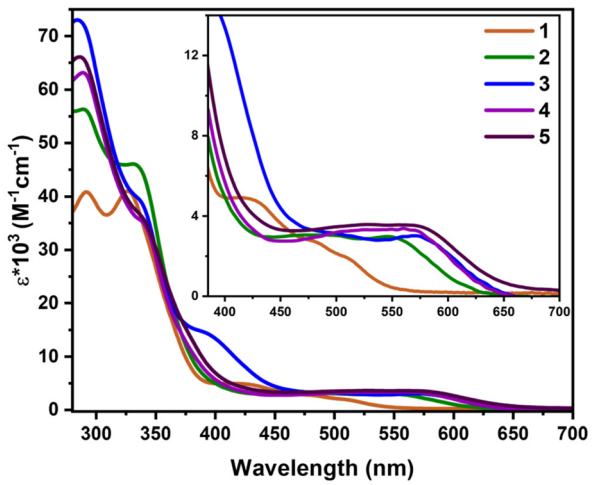

Fig. 3 UV-Vis absorption spectra of 1–5 measured in MeCN at room temperature (inset: MMLCT absorption bands of 1–5).

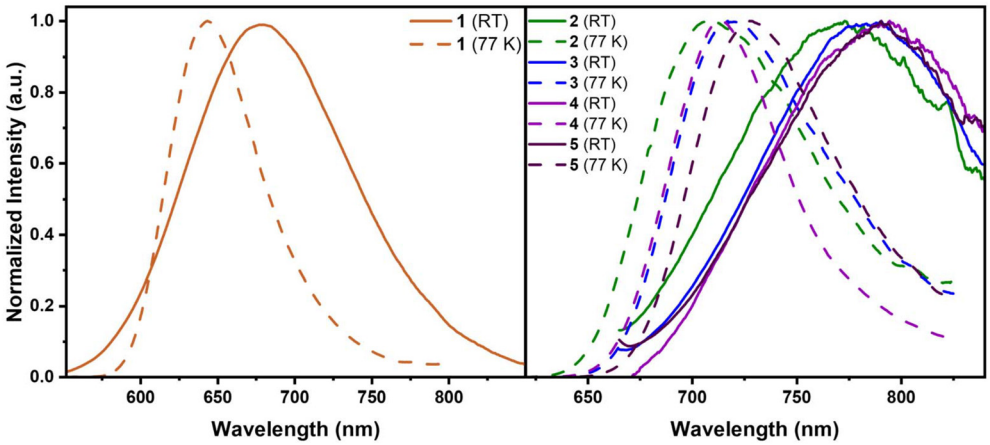

Fig. 4 (Left) Room temperature (MeCN, solid) and 77 K (butyronitrile, dashed) PL spectra of 1 following 500 nm excitation. (Right) Room temperature (550 nm, MeCN, solid) and 77 K (560 nm, butyronitrile, dashed) PL spectra of 2–5.

Static and time-resolved photoluminescence

Another means of characterizing the d_{z^2} orbital overlap in Pt(II) dimers is the photoluminescence (PL) energy. The PL spectra were measured across **1–5** at room temperature (RT) in MeCN and at 77 K in butyronitrile (Fig. 4), following excitation of the lowest energy MMCLT absorbance band. The PL spectra of **1**, previously established as arising from the ^{3}MMLCT excited state,[33,39,40] serve as a reference for the characterization of **2–5**. Finally, the PL intensity decays, fitted with a single exponential function, were collected to determine the lifetime of the emitting state using time-correlated single-photon counting experiments (Table 1).

At RT, **1–5** exhibit unstructured PL bands with peak maxima at 680 nm in **1**, extending to 775–793 nm in **2–5** (Table 1). By analogy with **1** and based on the characteristic unstructured emission profile, the PL from **2–5** is assigned as ^{3}MMLCT emission, with peak energies lower than those of previous 4tpbpy complexes. For instance, the ^{3}MMLCT PL of **1** is at least 1803 cm^{-1} higher in energy than **2–5**. This shift in PL energies suggests improved orbital overlap in the current structural motif.

The PL spectra of **1–5** were also measured at 77 K in butyronitrile (Fig. 4); the bands remained structureless, but all shifted hypsochromically due to the solvent's diminished ability to stabilize the charge-transfer excited state. The resulting thermally induced Stokes shift (Table 1) is larger in **2–5** compared to the moderate shift of **1**, suggesting that the new molecules possess a more polar ^{3}MMLCT excited state with increased charge separation, and potentially a more pronounced MMLCT charge transfer. Additionally, from the 77 K PL, the energy of the ^{3}MMLCT state was estimated by tangent analysis and compared with the ^{1}MMLCT state energy – measured by tangent analysis of the UV-Vis spectrum – to estimate the S_1–T_1 exchange energy ($\Delta E_{S\text{–}T}$) (Table 1; Fig. S11 and S12). The values of $\Delta E_{S\text{–}T}$ decrease from **1** to **5**, and may also reflect improved charge separation in the excited state.

Finally, the PL lifetimes (τ_{PL}) of **2–5** were measured following 570 nm excitation in MeCN and compared to **1** (λ_{ex} = 500 nm) (Table 1).[33] The shortest τ_{PL} of 2 ns was measured in **4**, with the lifetimes of **2**, **3**, and **5** being slightly lengthened to 6.8–7.7 ns. These excited state lifetimes are considerably shorter than the τ_{PL} of **1** (216.2 ns) and those of Pt(II) dimers with similar PL energies, which typically range from 100's of ns to the μs regime.[30,42,44–48] Proposed mechanisms for such rapid excited-state deactivation in **2–5** are described in the transient absorption section below.

Table 1 Characterization of the ^{3}MMLCT state by RT and 77 K PL energies and PL lifetimes

	λ_{PL} [a] (RT) (nm)	λ_{PL} [b] (77 K) (nm)	Thermally induced stokes shift [c] (cm^{-1})	S_1–T_1 exchange energy [d] (cm^{-1})	τ_{PL} [e] (ns)
1	679	644	812	1526.1	216.2 ± 0.3
2	775	709	1211	998.3	7.5 ± 0.3
3	789	720	1168	726.8	7.7 ± 0.3
4	792	713	1399	751.8	2.07 ± 0.01
5	793	729	1107	596.9	6.8 ± 0.2

[a] 298 K, MeCN, λ_{ex} = 500 (**1**)/550 (**2–5**) nm. [b] 77 K, butyronitrile, λ_{ex} = 500 (**1**)/560 (**2–5**) nm. [c] Measured based on peak maxima at RT and 77 K. [d] Energies based on tangent analysis at the blue-edge of the 77 K PL and the red edge of the MMLCT absorption. [e] 298K, MeCN, **1** (λ_{ex} = 500 nm; 1.2 mJ per pulse); **2–5** (λ_{ex} = 550 nm; 0.2 nJ per pulse).

Transient absorption spectroscopy – elucidation of the excited state trajectory

Due to the diminished excited-state lifetimes of **2–5**, analysis of the excited-state trajectory is limited to femtosecond transient absorption (fsTA) (MeCN, 550 nm excitation). The extended ^{3}MMLCT lifetime of **1**, as determined by τ_{PL}, necessitated experimentation with higher time resolution. The earlier decay processes of **1** were measured by fsTA, and the final relaxation of the ^{3}MMLCT state was characterized by nano-

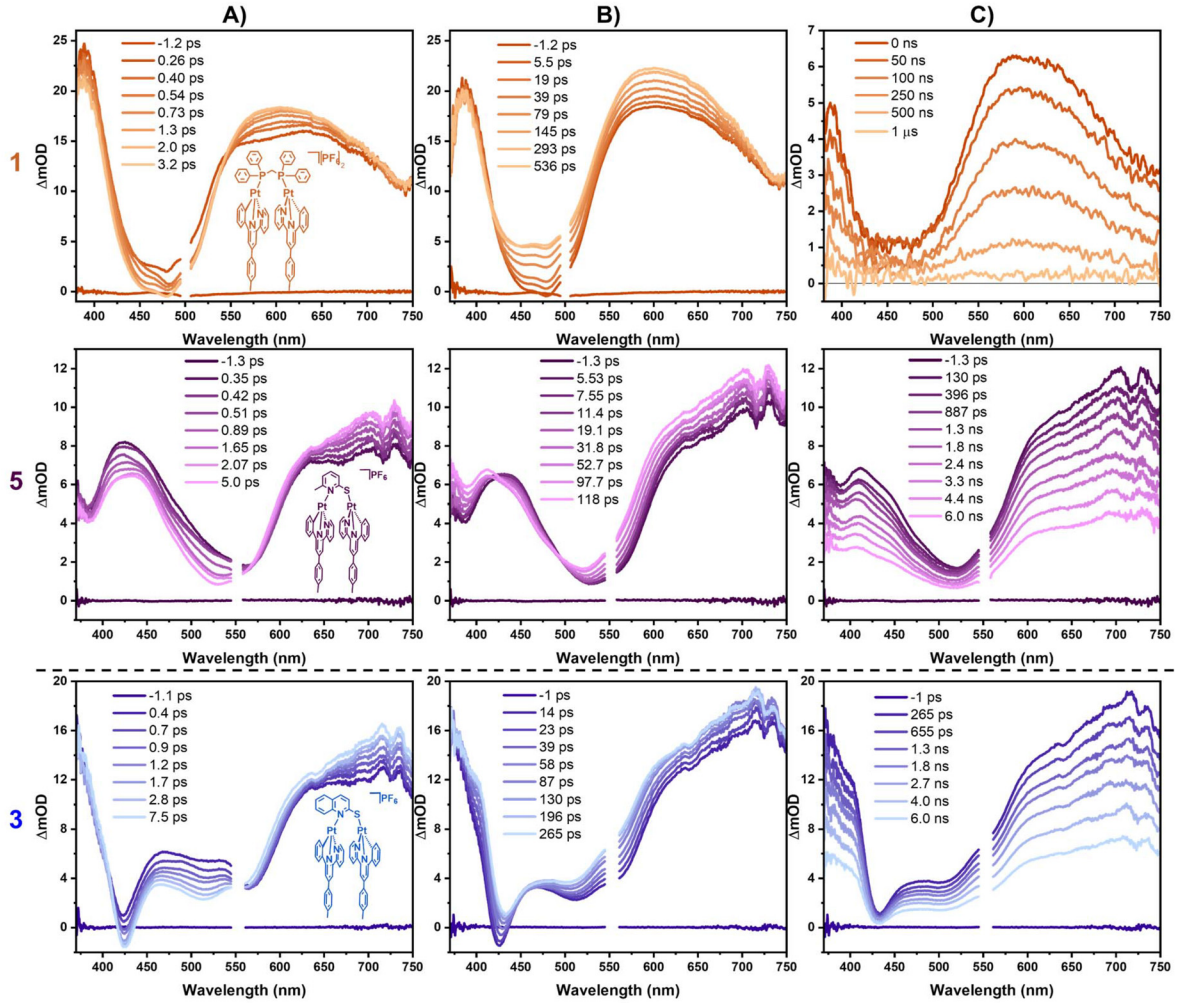

Fig. 5 Transient absorption difference spectra of complexes **1** (top, orange, 500 nm, fsTA: 1.5 μJ per pulse, nsTA: 1.2 mJ per pulse), **5** (middle, pink, 550 nm, 1.2 μJ per pulse), and **3** (bottom, blue, 550 nm, 1.2 μJ per pulse) in MeCN. The panels are separated by excited state process and are described by the following time constants: (A) τ_1 (^{1}MMLCT IC); (B) τ_2 (^{1}MMLCT → ^{3}MMLCT ISC), (C) τ_3 (^{3}MMLCT lifetime). All spectra were collected by fsTA except for panel C from **1**, which was collected by nsTA.

second transient absorption spectroscopy (nsTA), all in MeCN following 500 nm excitation. The combined difference spectra related to the relaxation of **1**, **3**, and **5** to the ground state following visible light excitation are displayed in Fig. 5, where distinct excited-state processes are highlighted in separate panels. The difference spectra of **2** and **4** mirror the relaxation of **5** and are displayed in Fig. S20 and S23. Except for **3**, each molecule exhibits a largely similar spectral shape and excited-state progression. The excited-state absorption (ESA) features of **2–5** are centred at lower energies than those of **1**, and their dynamics are characterized by shorter time constants. Complex **3**, however, exhibits a distinct spectral shape in the blue region, with a negative feature at 425 nm, corresponding to the additional band in the UV-vis spectrum proposed to originate from the π-orbitals of the bridge. The structured ESA aligns with previous reports in bidentate 2-quinolinethiol-bridged complexes, although the origin of the spectral features was not explicitly discussed in the prior investigation. Instead, the report suggested, based on DFT, that the bridging ligands contribute more to the frontier orbitals—and thus to the MMLCT transition—than in complexes bridged by 2-pyridinethiol. While the extended π-system of 2-quinolinethiol in **3** likely drives the increased ground-state absorption intensity at 425 nm and the resulting structure of the difference spectra, the impact of the bridging ligand on the excited-state progression was not previously explored and warrants computational investigation.

The difference spectra in Fig. 5 are dominated by two ESA features at all time points. In the high-energy region of the spectrum, a narrow absorption band is centred at 390 nm in **1** and red-shifted to 425 nm in **5** (ESA_1). Present in all complexes is a second broad ESA covering much of the visible spectrum and centred at 600 nm (**1**) and 675 nm in **2–5** (ESA_2). Starting the assignment of spectral progression with the final time points, panel **C** in Fig. 5 outlines the relaxation of the excited molecule to the ground state, observed by concomitant relax-

Table 2 Time constants associated with the decay pathway of the ^{1}MMLCT excited state in **1** (λ_{ex} = 500 nm; 1.5 μJ per pulse) and **2–5** (λ_{ex} = 550 nm; 1.2 μJ per pulse) in MeCN

	τ_1 (ps) (^{1}MMLCT IC)	τ_2 (ps) (ISC)	τ_3 (ns) (^{3}MMLCT)
1	0.45 ± 0.03	105 ± 5	211 ± 3
2	1.0 ± 0.1	59 ± 7	3.5 ± 0.2
3	0.9 ± 0.3	54 ± 8	4.5 ± 0.2
4	0.99 ± 0.05	55 ± 2	2.0 ± 0.3
5	1.03 ± 0.08	52 ± 8	4.1 ± 0.7

ation of both ESA_1 and ESA_2. The time constants associated with this relaxation are defined as τ_3 in Table 2. In **1**, this has previously been assigned to the relaxation of the ^{3}MMLCT state, based on agreement between the excited-state and PL lifetimes. This remains true for the relaxation reported here in MeCN, as τ_3 was determined to be 211 ns. While **2**, **3**, and **5** do not completely return to the ground state in the time window of the experiment, and therefore the value of τ_3 discerned from single-wavelength kinetics is merely an estimate, the relative agreement between τ_3 and τ_{PL} in Table 2 and Table 1, respectively, confirms the assignment of τ_3 as the ^{3}MMLCT lifetime in **2–5**. The spectral shape in Fig. 5C thus corresponds to the absorption of the ^{3}MMLCT excited state.

The spectral progression directly preceding this in Fig. 5B must then correspond to the population of the ^{3}MMLCT excited state. The time constants associated with this time window, nominally τ_2, are defined in Table 2. In agreement with previous reports of **1** in THF, the growth of ESA_2 persists until the spectral shape mirrors the difference spectra associated with the ^{3}MMLCT state. This growth was assigned as the ^{1}MMLCT → ^{3}MMLCT intersystem crossing with an associated time constant of 155 ps. Here in MeCN, **1** undergoes this process slightly faster with a τ_2 of 105 ps. Previous reports of Pt(POP) attribute a similar solvent-mediated acceleration of ISC in MeCN to the stabilization of a higher-energy charge-transfer state, such that it can energetically mediate the ISC;[6] however, the spectral progression in THF and MeCN appears otherwise identical, suggesting that an intermediate state is not at play, and the reduced rate in MeCN is due to solvent-polarity-mediated reduction of the ΔE_{S-T}, calculated in Table S1. The corresponding growth of ESA_2 in **2–5** is characterized by a τ_2 of 52–59 ps (Table 2), and the agreement in spectral progression with **1** makes it most likely that Fig. 5B also describes the ^{1}MMLCT → ^{3}MMLCT ISC. That said, the progression of ESA_1 in **3** and **5** differs slightly during this time window compared to **1**. The intensity of ESA_1 in the model complex diminishes, whereas in **3** and **5**, the feature blue shifts while the intensity appears unchanged. The impetus for such a shift is unclear, but the successful fitting of single-wavelength kinetic decays in the corresponding time region by monoexponential functions seemingly precludes additional excited-state processes.

Finally, panel **A** describes a rapid state transfer with time constants (τ_1) of 450 fs (**1**) and approximately 1 ps in **2–5**. The presence of an isosbestic point suggests rapid internal conversion within the ^{1}MMLCT manifold. As previously described, Pt(II) dimers with MMLCT photophysics exhibit two charge-transfer transitions of similar energy, arising from splitting of the CML π* into in-phase and out-of-phase components (Fig. 1). Given that the excitation energy utilized for fsTA experiments falls within the MMLCT absorption band and should preclude population of higher energy singlet states, the most likely cause of the early state transfer observed in panel **A** is the ^{1}MMLCT(out-of-phase) → ^{1}MMLCT (in-phase) IC. It would follow that this IC would have a longer time constant in the thiol-bridged complexes, as the diminished Pt–Pt distance would cause increased splitting between the π* orbitals, and therefore increase the energy separation between ^{1}MMLCT states. That said, further computational studies are required to verify this assignment, as this process was likely present but not addressed in the relaxation of **1** in THF.[33]

Of note is the rapid deactivation of the excited state manifold in **2–5** compared to **1**. This is evident in both the proposed ISC rate (τ_2) and the relaxation of the ^{3}MMLCT state, as described by τ_{PL} in the previous section and τ_3 from the fsTA experiments. Assuming the assignment of τ_2 as the ISC rate is accurate, the rate decreases with decreasing ΔE_{S-T} (Table 1), as anticipated from energy gap behaviour. However, on a plot of ΔE_{S-T} *vs.* $\ln(K_{ISC})$, in which the linear fitting was clearly established for **2–5** only, there is good agreement between the new molecules, but **1** deviates considerably from the trendline (Fig. S26). This, along with the observation that **2–5** have appreciably shorter ^{3}MMLCT relaxation times than complexes with similar PL energies, suggests that the energy gap law alone does not account for the observed rates; other factors must contribute. One such factor, as previously mentioned in **3**, is the potential orbital mixing of the π-conjugated bridge with the MMLCT transition, which is not possible in **1**. While not previously reported in complexes bridged by thiol–pyridines, this could lead to faster rates by introducing additional vibrational modes into the transition of the new molecules and should be examined computationally. More significantly, it should be considered that **2–5** are completely asymmetric, whereas the previous Pt(II) dimers mentioned here are of pseudo-C_2 symmetry. At low symmetry, all excited-state processes become fully allowed and could provide a mechanism to reduce the associated time constants. However, further characterization by both fs broadband transient absorption with improved time resolution and theoretical analyses is required to better understand the excited-state decay processes in **2–5**.

Conclusions

Four novel Pt(II) dimers (**2–5**) bridged by thiol–pyridine and thiol–quinoline motifs and cyclometalated by the tridentate ligand, 4-tolyl-6-phenyl-2,2′-bipyridine, were successfully prepared. The red shifts in the UV-Vis and PL features in these molecules compared to previous structural motifs are indicative of Pt(II) dimers with improved d_{z^2}–d_{z^2} orbital overlap. The

excited-state trajectory following photoexcitation mirrors that of previously studied Pt(II) dimers with the tridentate motif, albeit with shorter time constants. Specifically, a proposed 52–59 ps ^{1}MMLCT → ^{3}MMLCT ISC occurs more rapidly than in model complex **1**, followed by relaxation of the ^{3}MMLCT excited state of **2–5** on the 2–7 ns timescale. The accelerated dynamics in **2–5** can be attributed in part to reduced energy separations between states, though the C_1 symmetry of the new molecules could also hasten excited-state processes. Such structural motifs have yet to be examined for their role in the propagation of the CVWP and could provide valuable insight into the role of structure on vibronic coherence in Pt(II) dimers.

Author contributions

The manuscript was written through the contributions of all authors. All authors have approved the final version of the manuscript.

Conflicts of interest

There are no conflicts to declare.

Data availability

The raw experimental and characterization data will be shared upon request.

Supplementary information (SI): contains substantial details on structural characterization, tangent analysis of absorption and photoluminescence spectra, and single-wavelength kinetics. See DOI: https://doi.org/10.1039/d6dt00411c.

Acknowledgements

This work was funded by the National Science Foundation under Award CHE-2247822. L. J. D. and A. P. F. are supported by the U.S. Department of Energy, Office of Science, Office of Basic Energy Sciences, under Award DE-SC0011979.

References

1 R. M. van der Veen, J. J. Kas, C. J. Milne, V.-T. Pham, A. El Nahhas, F. A. Lima, D. A. Vithanage, J. J. Rehr, R. Abela and M. Cherugi, *Phys. Chem. Chem. Phys.*, 2010, **12**, 5551–5561.
2 R. M. Van Der Veen, A. Cannizzo, F. Van Mourik, A. Vlček and M. Chergui, *J. Am. Chem. Soc.*, 2011, **133**, 305–315.
3 T. J. Penfold, B. F. E. Curchod, I. Tavernelli, R. Abela, U. Rothlisberger and M. Chergui, *Phys. Chem. Chem. Phys.*, 2012, **14**, 9444–9450.
4 R. Monni, G. Auböck, D. Kinschel, K. M. Aziz-Lange, H. B. Gray, A. Vlček and M. Chergui, *Chem. Phys. Lett.*, 2017, **683**, 112–120.
5 G. Levi, M. Pápai, N. E. Henriksen, A. O. Dohn and K. B. Møller, *J. Phys. Chem. C*, 2018, **122**, 7100–7119.
6 R. Monni, G. Capano, G. Auböck, H. B. Gray, A. Vlcek, I. Tavernelli and M. Chergui, *Proc. Natl. Acad. Sci. U. S. A.*, 2018, **115**, E6396–E6403.
7 K. Haldrup, G. Levi, E. Biasin, P. Vester, M. G. Laursen, F. Beyer, K. S. Kjær, T. B. Van Driel, T. Harlang, A. O. Dohn, R. J. Hartsock, S. Nelson, J. M. Glownia, H. T. Lemke, M. Christensen, K. J. Gaffney, N. E. Henriksen, K. B. Møller and M. M. Nielsen, *Phys. Rev. Lett.*, 2019, **122**, DOI: 10.1103/PhysRevLett.122.063001.
8 P. Karak, K. Ruud and S. Chakrabarti, *J. Phys. Chem. Lett.*, 2021, **12**, 9768–9773.
9 J. V. Lockard, A. A. Rachford, G. Smolentsev, A. B. Stickrath, X. Wang, X. Zhang, K. Atenkoffer, G. Jennings, A. Soldatov, A. L. Rheingold, F. N. Castellano and L. X. Chen, *J. Phys. Chem. A*, 2010, **114**, 12780–12787.
10 S. Cho, M. W. Mara, X. Wang, J. V. Lockard, A. A. Rachford, F. N. Castellano and L. X. Chen, *J. Phys. Chem. A*, 2011, **115**, 3990–3996.
11 D. B. Lingerfelt, P. J. Lestrange, J. J. Radler, S. E. Brown-Xu, P. Kim, F. N. Castellano, L. X. Chen and X. Li, *J. Phys. Chem. A*, 2017, **121**, 1932–1939.
12 J. J. Radler, D. B. Lingerfelt, F. N. Castellano, L. X. Chen and X. Li, *J. Phys. Chem. A*, 2018, **122**, 5071–5077.
13 A. J. S. Valentine, J. J. Radler, A. Mills, P. Kim, F. N. Castellano, L. X. Chen and X. Li, *J. Chem. Phys.*, 2019, **151**, 114303.
14 L. Mewes, R. A. Ingle, S. Megow, H. Böhnke, E. Baranoff, F. Temps and M. Chergui, *Inorg. Chem.*, 2020, **59**, 14643–14653.
15 P. Kim, M. S. Kelley, A. Chakraborty, N. L. Wong, R. P. Van Duyne, G. C. Schatz, F. N. Castellano and L. X. Chen, *J. Phys. Chem. C*, 2018, **122**, 14195–14204.
16 P. Kim, A. J. S. Valentine, S. Roy, A. W. Mills, A. Chakraborty, F. N. Castellano, X. Li and L. X. Chen, *J. Phys. Chem. Lett.*, 2021, **12**, 6794–6803.
17 N. P. Weingartz, M. W. Mara, S. Roy, J. Hong, A. Chakraborty, S. E. Brown-Xu, B. T. Phelan, F. N. Castellano and L. X. Chen, *J. Phys. Chem. A*, 2021, **125**, 8891–8898.
18 D. Leshchev, A. J. S. Valentine, P. Kim, A. W. Mills, S. Roy, A. Chakraborty, E. Biasin, K. Haldrup, D. J. Hsu, M. S. Kirschner, D. Rimmerman, M. Chollet, J. M. Glownia, T. B. van Driel, F. N. Castellano, X. Li and L. X. Chen, *Angew. Chem., Int. Ed.*, 2023, **62**(28), e202304615, DOI: 10.1002/anie.202304615.
19 P. Kim, S. Roy, A. J. S. Valentine, X. Liu, S. Kromer, T. W. Kim, X. Li, F. N. Castellano and L. X. Chen, *Chem. Sci.*, 2024, **15**, 14766–14777.
20 T. W. Kim, P. Kim, A. W. Mills, A. Chakraborty, S. Kromer, A. J. S. Valentine, F. N. Castellano, X. Li and L. X. Chen, *J. Phys. Chem. C*, 2022, **126**, 11487–11497.
21 P. Kim, S. Kromer, N. Durand, F. N. Castellano and L. X. Chen, *J. Phys. Chem. Lett.*, 2025, **16**, 11745–11751.

22 S. Rafiq, N. P. Weingartz, S. Kromer, F. N. Castellano and L. X. Chen, *Nature*, 2023, **620**, 776–781.
23 M. W. Mara, D. Leshchev, N. P. Weingartz, A. M. Chan, A. K. Nijhawan, A. J. S. Valentine, X. Liu, S. Kromer, D. Hsu, P. Kim, E. Biasin, T. B. van Driel, F. N. Castellano, X. Li and L. X. Chen, *J. Phys. Chem. Lett.*, 2025, **16**, 7120–7126.
24 K. Haldrup, A. O. Dohn, M. L. Shelby, M. W. Mara, A. B. Stickrath, M. R. Harpham, J. Huang, X. Zhang, K. B. Møller, A. Chakraborty, F. N. Castellano, D. M. Tiede and L. X. Chen, *J. Phys. Chem. A*, 2016, **120**, 7475–7483.
25 G. D. Scholes, G. R. Fleming, L. X. Chen, A. Aspuru-Guzik, A. Buchleitner, D. F. Coker, G. S. Engel, R. Van Grondelle, A. Ishizaki, D. M. Jonas, J. S. Lundeen, J. K. McCusker, S. Mukamel, J. P. Ogilvie, A. Olaya-Castro, M. A. Ratner, F. C. Spano, K. B. Whaley and X. Zhu, *Nature*, 2017, **543**, 647–656.
26 A. A. Rachford and F. N. Castellano, *Inorg. Chem.*, 2009, **48**, 10865–10867.
27 A. Chakraborty, J. C. Deaton, A. Haefele and F. N. Castellano, *Organometallics*, 2013, **32**, 3819–3829.
28 A. Chakraborty, J. E. Yarnell, R. D. Sommer, S. Roy and F. N. Castellano, *Inorg. Chem.*, 2018, **57**, 1298–1310.
29 S. E. Brown-Xu, M. S. J. Kelley, K. A. Fransted, A. Chakraborty, G. C. Schatz, F. N. Castellano and L. X. Chen, *J. Phys. Chem. A*, 2016, **120**, 543–550.
30 S. Roy, A. A. Lopez, J. E. Yarnell and F. N. Castellano, *Inorg. Chem.*, 2022, **61**, 121–130.
31 S. Kromer, S. Roy, J. E. Yarnell, C. M. Taliaferro and F. N. Castellano, *Dalton Trans.*, 2023, **52**, 4008–4016.
32 A. W. Mills, A. J. S. Valentine, K. Hoang, S. Roy, F. N. Castellano, L. X. Chen and X. Li, *J. Phys. Chem. A*, 2021, **125**, 9438–9449.
33 S. Kromer, X. Yang, R. Alameh, E. O. Danilov, M. C. Rosko, A. M. May, J. P. Wheeler, X. Li and F. N. Castellano, *Inorg. Chem.*, 2025, **64**, 24634–24645.
34 P. Pander, Y. M. Dikova, E. V. Puttock and J. A. G. Williams, *Inorg. Chem. Front.*, 2024, **11**, 7545–7551.
35 B. Ma, P. I. Djurovich, M. Yousufuddin, R. Bau and M. E. Thompson, *J. Phys. Chem. C*, 2008, **112**, 8022–8031.
36 B. Ma, J. Li, P. I. Djurovich, M. Yousufuddin, R. Bau and M. E. Thompson, *J. Am. Chem. Soc.*, 2005, **127**, 28–29.
37 C. Zhou, L. Yuan, Z. Yuan, N. K. Doyle, T. Dilbeck, D. Bahadur, S. Ramakrishnan, A. Dearden, C. Huang and B. Ma, *Inorg. Chem.*, 2016, **55**, 8564–8569.
38 B. Ma, P. I. Djurovich, S. Garon, B. Alleyne and M. E. Thompson, *Adv. Funct. Mater.*, 2006, **16**, 2438–2446.
39 S. W. Lai, M. C. W. Chan, T. C. Cheung, S. M. Peng and C. M. Che, *Inorg. Chem.*, 1999, **38**, 4046–4055.
40 T.-C. Cheung, K.-K. Cheung, S.-M. Peng' and C.-M. Che, *J. Chem. Soc., Dalton Trans.*, 1996, 1645–1651.
41 M. A. Esteruelas, S. Moreno-Blázquez, M. Oliván and E. Oñate, *Inorg. Chem.*, 2024, **63**, 14482–14494.
42 A. Yu, W. Jiang, Y. Shen and Y. Zhang, *Cryst. Growth Des.*, 2025, **25**, 1872–1879.
43 M. Gao, W. P. To, G. S. M. Tong, L. Du, K. H. Low, Z. Tang, W. Lu and C. M. Che, *Angew. Chem., Int. Ed.*, 2025, **64**, e202414411, DOI: 10.1002/anie.202414411.
44 K. W. Lo, C. H. Tsang, S. Xu, G. Cheng, X. Chang, L. Duan and C. M. Che, *Angew. Chem., Int. Ed.*, 2026, **65**, e19762, DOI: 10.1002/anie.202519762.
45 L. Yuan, H. Yao, Y. Shen and Y. Zhang, *Dalton Trans.*, 2024, **53**, 5125–5132.
46 I. G. de Segura, D. G. de Segura, M. Hasler, M. T. Moreno, E. Lalinde, M. Nieddu, R. D. Costa and J. Fernandez-Cestau, *J. Mater. Chem. C Mater.*, 2025, **13**, 15002–15012, DOI: 10.1039/D5TC01319D.
47 P. Pander, M. T. Walden, R. J. Salthouse, A. Sil, D. S. Yufit, F. B. Dias and J. A. G. Williams, *J. Mater. Chem. C Mater.*, 2023, **11**, 15335–15346.
48 Y. Zhu, K. Luo, L. Zhao, H. Ni and Q. Li, *Dyes Pigm.*, 2017, **145**, 144–151.
49 H. J. Park, C. L. Boelke, P. H. Y. Cheong and D. H. Hwang, *Inorg. Chem.*, 2022, **61**, 5178–5183.
50 T. Koshiyama, A. Omura and M. Kato, *Chem. Lett.*, 2004, **33**, 1386–1387.
51 F. Krohnke, *Synthesis*, 1976, 1–24.
52 S. C. F. Kui, I. H. T. Sham, C. C. C. Cheung, C. W. Ma, B. Yan, N. Zhu, C. M. Che and W. F. Fu, *Chem. – Eur. J.*, 2007, **13**, 417–435.